Realizing Record High Performance in n-type Bi_2Te_3-Based Thermoelectric Materials

Bin Zhu[a,b,†], Xixi Liu[a,†], Qi Wang[c,†], Yang Qiu[a], Zhong Shu[a], Zuteng Guo[a], Yao Tong[a], Juan Cui[a], Meng Gu[c], Jiaqing He[a,d,*]

[a]Shenzhen Key Laboratory of Thermoelectric Materials and Department of Physics, Southern University of Science and Technology, Shenzhen, 518055, China
[b]School of Physics and Technology, Wuhan University, Wuhan, 430072, China
cDepartment of Materials Science and Engineering and Shenzhen Engineering Research Center for Novel Electronic Information Materials and Devices, Southern University of Science and Technology, Shenzhen, 518055, China
dMOE Key Laboratory of Energy Conversion and Storage Technologies, Southern University of Science and Technology, Shenzhen, 518055, China

†These authors contribute equally
*Correspondence: hejq@sustech.edu.cn

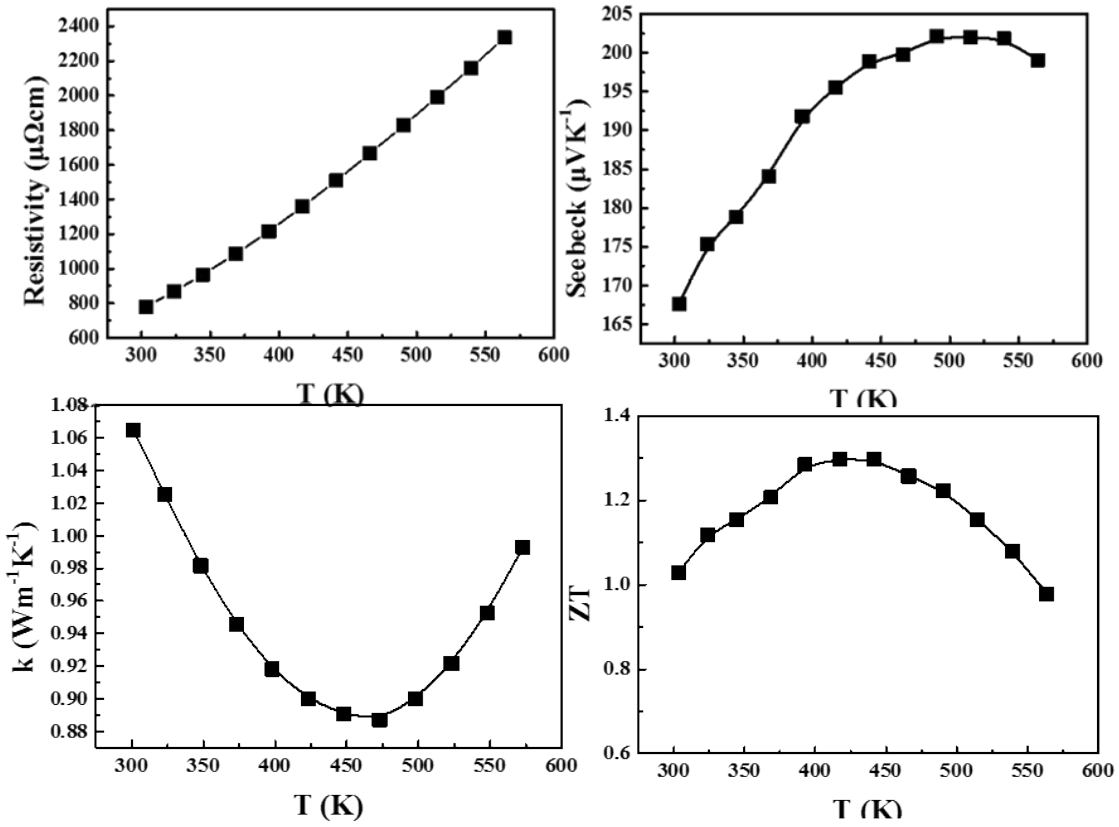

Figure S1 (a) σ, (b) S, (c) κ (e) and (d) ZT value.

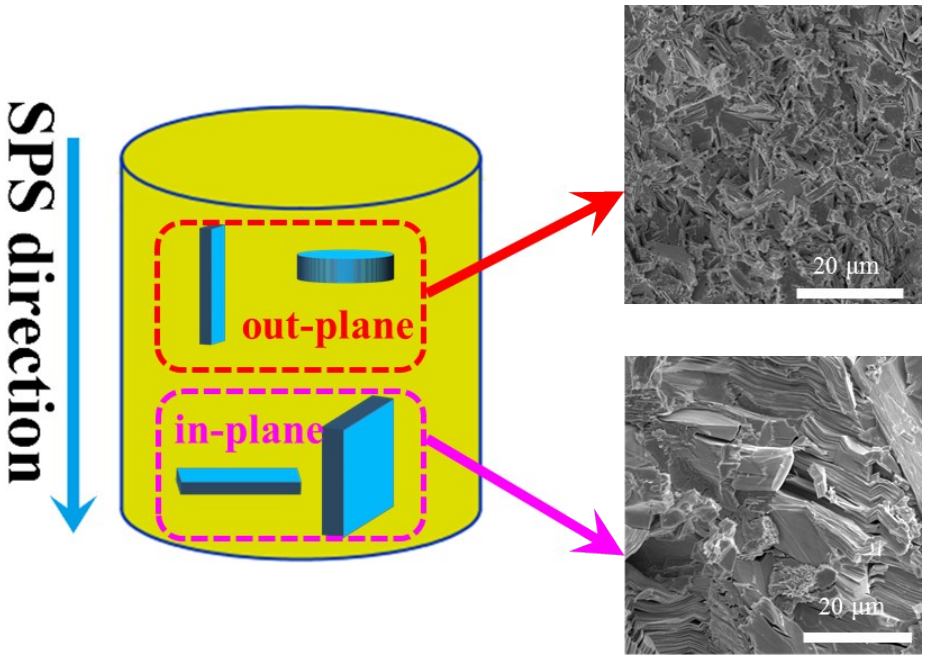

Figure S2 Schematic illustration of the preparation of samples for measuring TE properties and SEM images for out-plane and in-plane directions.

The SEM image along out-plane structure displayed a relatively isotropic microstructure. While the strong layered structure can be observed along the in-plane direction, which indicate a highly preferred orientation.

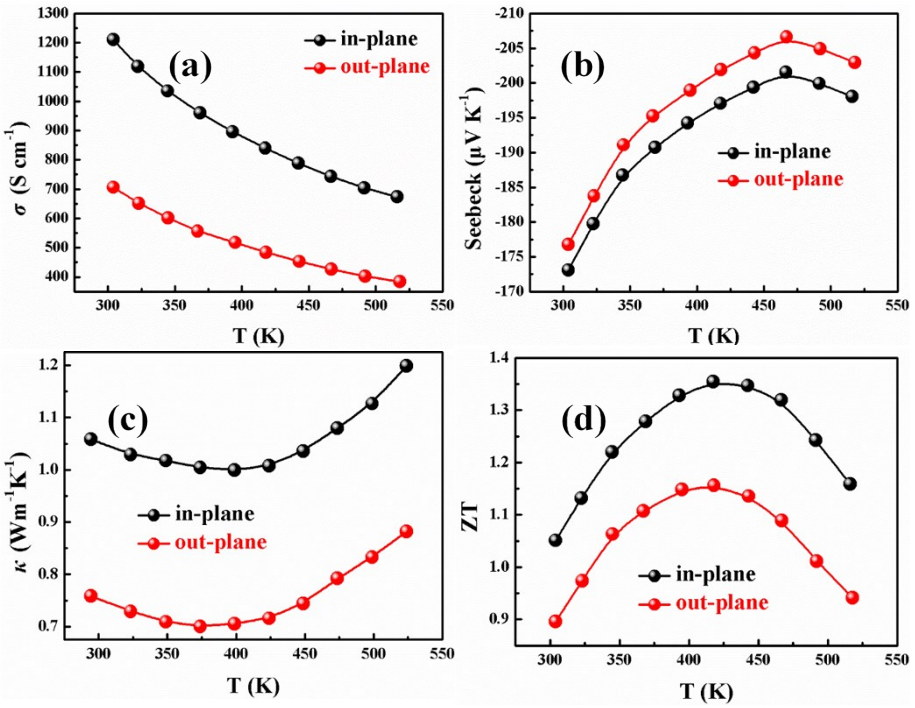

Figure S3 The in-plane and out-plane temperature dependence of (a) electrical conductivity, (b) Seebeck coefficient (c) thermal conductivity and (d) ZT values for 0.2Sb sample.

As well known, the anisotropy of Bi_2Te_3 based alloy is very strong. Generally, their

electrical and thermal conductivities along the a-axis (in the c-plane, vertical to SPS direction in this work) are approximately four and two times higher, respectively, than those along the c-axis (parallel to SPS direction in this work) of Bi_2Te_3. However, the Seebeck coefficient is less dependent on the crystallography. Therefore, we should measure the electrical and the thermal properties along the same direction to avoid the over-estimation of TE properties. We used 0.2Sb sample as an example to illustrate as shown in **Figure S3**. It can be observed that the in-plane properties is much higher than the out-plane properties. Therefore, the TE properties of all samples stated above were measured along the direction vertical to the SPS (in-plane) in the main text.

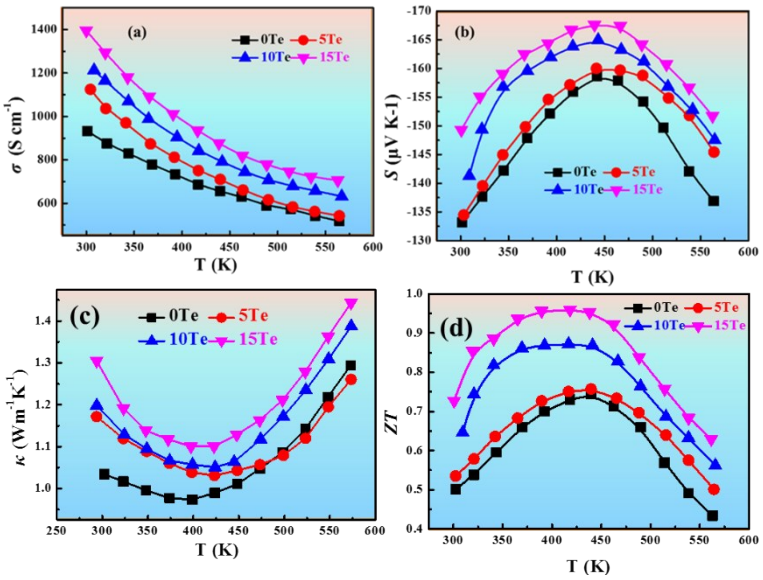

Figure S4 (a) σ, (b) S (c) κ and (d) ZT value of $Bi_2Te_{2.7}Se_{0.3}$ + x% Te sample, where x=0, 5, 10 and 15.

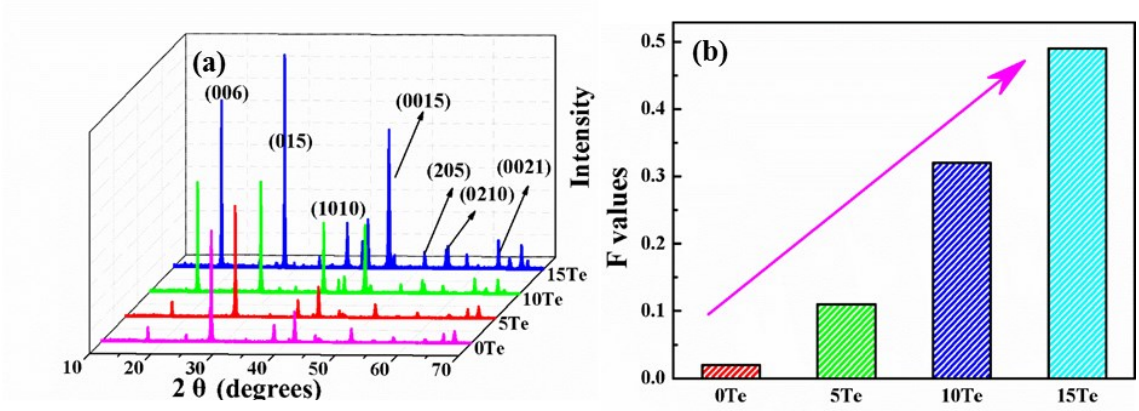

Figure S5 (a)XRD patterns vertical to the press direction and (b) orientation factor F of $Bi_2Te_{2.7}Se_{0.3}$ + x% Te (x=0, 5, 10, 15).

In order to understand the effect of liquid Te phase sintering on the preferred orientation

for n-type $Bi_2(Te, Se)_3$ alloys, we measured the in-plane XRD patterns of $Bi_2Te_{2.7}Se_{0.3}$ + x wt.% Te (x=0, 5, 10, 15) products, as shown in **Figure S5**(a). As can be seen, all the reflection peaks can be indexed to a rhombohedral phase (JCPDS#50-0954). With increasing Te content, the enhanced intensity of the (001) peak and almost invariable intensity of the (015) peak could be observed, indicating the (001) is the preferred orientation. The orientation degree F of the (001) planes is used to roughly evaluate the texture degree of samples,[1] as plotted in Figure S5(b). The values of F rapidly rise from 0.02 for 0Te sample to 0.47 for 15Te sample, demonstrating that the preferred crystalline orientation is enhanced remarkably by increasing Te content. The enhanced preferred orientation may be the result of promoted plane slipping and recrystallization by liquid Te during the SPS process, as reported in p-type $Bi_{0.5}Sb_{1.5}Te_3$ sample.[2]

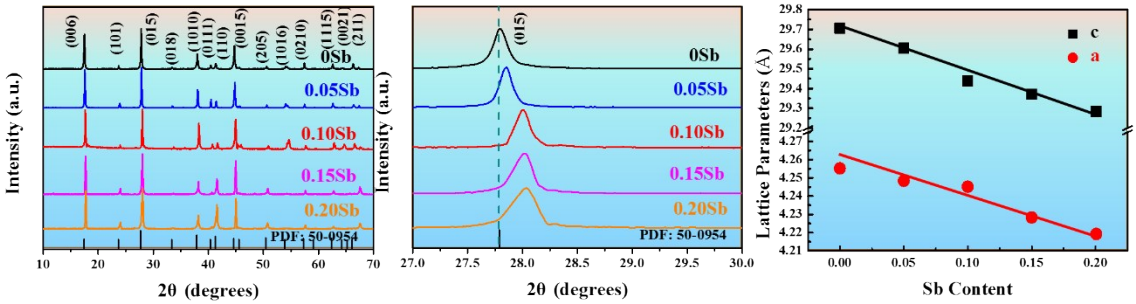

Figure S6 (a) The XRD patterns (b) the enlarged view of (015) peaks and (c) the calculated lattice parameters of all Sb doped samples.

According to the mechanism of point defect formation, Sb could suppress the formation of vacancy in n-type Bi-Te-Se system, so the decreased electron concentration could be expected. Therefore, we doped Sb into 15Te sample, the XRD patterns of all Sb doped samples are shown in **Figure S6**(a), in which all diffraction peaks could be indexed as PDF#51-0643 and the intensity of (00l) peaks are very similar with 0Sb sample, which may indicate the Sb-doping shows a little effect on preferred orientation. This find is important because it is beneficial for maintaining carrier mobility and thus electrical conductivity. Figure S6 (b) shows the enlarged view of (015) peaks shifting for different Sb containing samples. The calculated lattice parameters are consistent with the Vegard's law (Figure S6 (c)), which demonstrated that the Sb has been successfully doped into matrix. It should be mentioned that the calculated of F values for all Sb samples are all around 0.45, which further suggest the Sb doping have little effect on

the texturing.

The calculation of L number

For metals or heavily doped degenerate semiconductors, *L* is constant and equals to $2.44 \times 10^{-8} W\Omega K^{-2}$, whereas it approaches $1.5 \times 10^{-8} W\Omega K^{-2}$ for nondegenerate semiconductors. On the basis of the single parabolic band (SPB) model with acoustic phonon scattering dominating, the Lorenz number, *L*, can be derived from the following equations:

$$L = \left(\frac{k_B}{e}\right)^2 \left(\frac{(\lambda + \frac{7}{2})F_{r+\frac{5}{2}}(\eta)}{(\lambda + \frac{3}{2})F_{r+\frac{1}{2}}(\eta)} - \left[\frac{(\lambda + \frac{5}{2})F_{r+\frac{3}{2}}(\eta)}{(\lambda + \frac{3}{2})F_{r+\frac{1}{2}}(\eta)} \right]^2 \right) \quad \text{(S1)}$$

$$F_n(\eta) = \int_0^\infty \frac{x^n}{1 + e^{x-\eta}} dx \quad \text{(S2)}$$

$$S = \pm \frac{k_B}{e} \left(\frac{(\lambda + \frac{5}{2})F_{\lambda+\frac{3}{2}}(\eta)}{(\lambda + \frac{3}{2})F_{\lambda+\frac{1}{2}}(\eta)} - \eta \right) \quad \text{(S3)}$$

Where k_B is the Boltzmann constant, e is the electron charge, λ is the scattering parameter which equals to -0.5 for acoustic phonon scattering, $F_n(\eta)$ is the n-th order Fermi integral and η is the reduced Fermi energy, which can be calculated from the measured Seebeck coefficient according to Equation S3. The results are shown in the **Figure S7**.

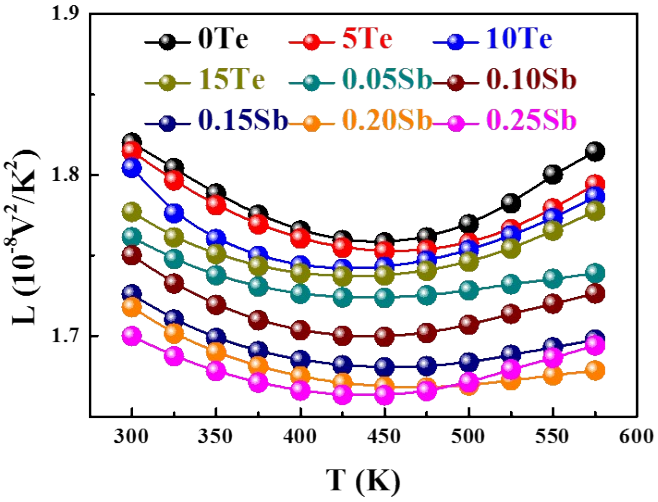

Figure S7 The Lorentz number for all samples.

The calculation of E_{def} and κ_b

At first the minor carrier (hole) concentration should be calculated.

Only the law of mass action at temperature T, the electrons (n) and holes (p) concentration is shown here,

$$n(T)p(T) = AT^3 exp(-E_g/k_BT) \qquad \text{(S4)}$$

where n and κ_B are the electron carrier concentration and Boltzmann constant respectively, and A is temperature-independent constant. Based on n and p data at 300 K, A can be calculated and listed at Table R1. At temperatures above 300 K, material's intrinsic excitation has to be considered, the equation S1 can be re-written as

$$(n_{300K} + \Delta)(p_{300K} + \Delta) = AT^3 exp(-E_g/k_BT) \qquad \text{(S5)}$$

where Δ represents the excited concentration of electron-hole pairs at temperature T. The actual n and p values above 300 K are then calculated as shown in **Figure S8**. In p-type Bi_2Te_3–based materials, acoustic phonon scattering is also the dominant carrier scattering mechanism around 300 K. Thus, the hole mobility (μ_p) also obey the relationship of $\mu_p \sim T^{-3/2}$. Based on Figure S8(b), we found that the calculated hole concentration (p) for all samples varies as with the empirical relationship of $p \sim T^{7.5}$. Thus, a qualitative expression between μ_e and n_e is derived as $\mu_p \approx Bn^{-1/5}$, where B is a temperature independent constant for a fixed composition (Table S2).

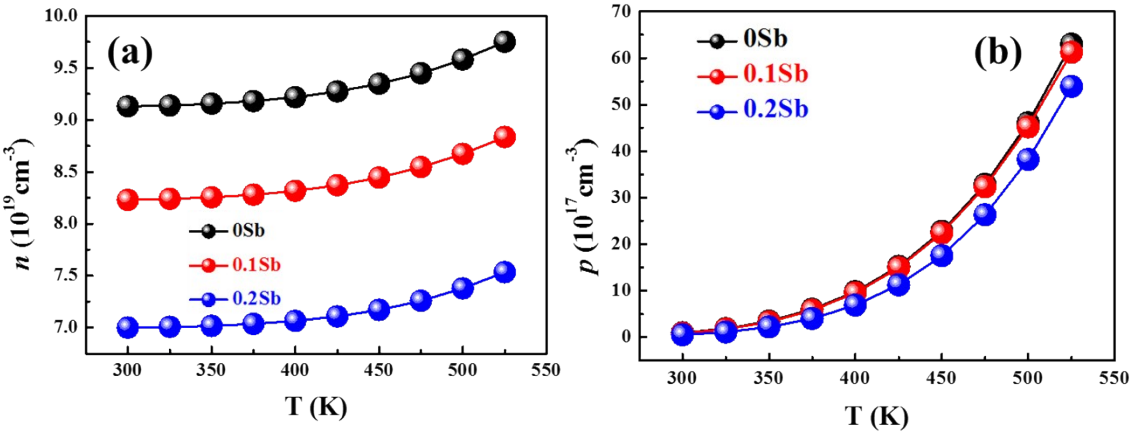

Figure S8 Temperature dependence of calculated (a) *n* and (b) *p*.

The Deformation potential E_{def} calculation:

Based on the electron and hole concentration and mobility calculated above, Deformation potential E_{def} in valance and conduction band can be roughly estimated by Equation S3, when the acoustic phonon scattering is dominant

$$E_{def}^{2} = \frac{(8\pi)^{0.5}(h/2\pi)^{4} e\rho v_L^2}{3\left(m_b^*\right)^{2.5}(k_B T)^{1.5}\mu_i} \qquad \text{(S6)}$$

Where ρ and v_L are density and longitudinal velocity of sound, i=electron or hole, m_b^* is the single valley effective $m_b^* = m^* N_v^{-2/3}$, N_v is the multiple degenerate valleys. The calculated E_{def} in valance and conduction are shown in **Figure 2(c) and (d)**, respectively.

The bipolar thermal conductivity calculation:

The electron partial electrical conductivity σ_e and bipolar can be calculated by the following equation:

$$k_b = \left(\frac{k_B}{e}\right)^2 T(5 + 2\lambda + \frac{E_g}{k_B T})^2 \frac{\sigma_e}{1 + \sigma_e/\sigma_h} \qquad \text{(S7)}$$

By subtracting the κ_b value from the $\kappa_l+\kappa_b$ (shown in Figure 1(e)), the experiment κ_l value can be attained (shown in Figure 4(a), orange plots).

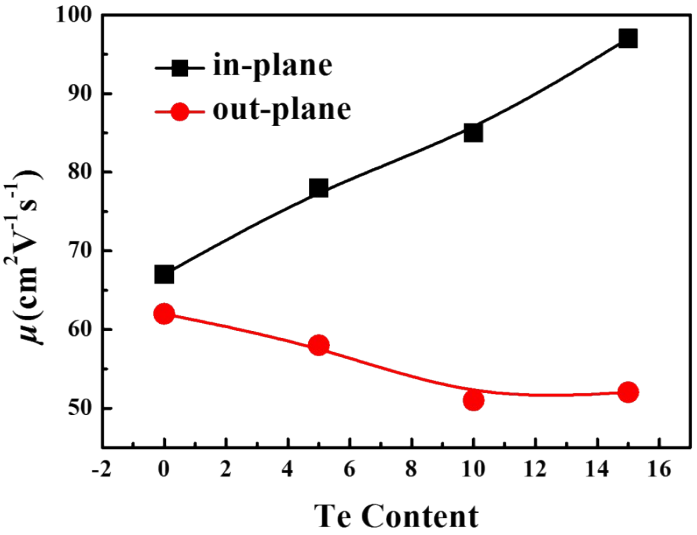

Figure S9 The in-plane and out-plane carrier mobility as a function of Te content.

In this work, the μ is simultaneously influenced by the texturing and potential well. we measured the out-plane μ as shown in **Figure S9**. As can be seen, Indeed, the decreased μ along the out-plane direction is the result of potential well and texturing, it is difficult to separating respective contribution because we could not get a sample only has potential well or texturing. However, μ is apparently increased along in-plane direction (texturing direction), which is the result of increased texturing. Generally speaking, the potential well could not provide positive effect on carrier mobility due to the localization of carrier. But in this work potential well is accompanied with texturing, which significantly improve mobility along the in-plane direction. As a result, potential well enhance S and texturing improve σ, a high PF could be obtained in our samples.in additional Te series samples.

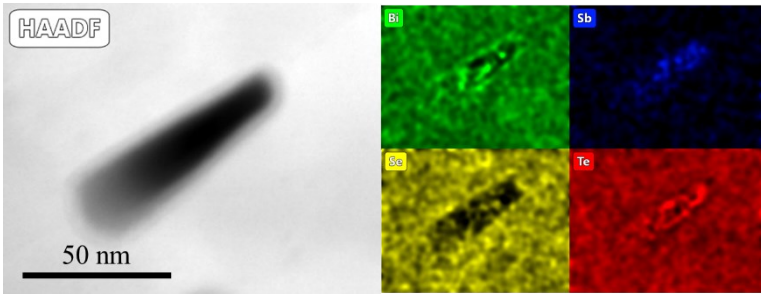

Figure S10 The Sb-rich nano second phase.

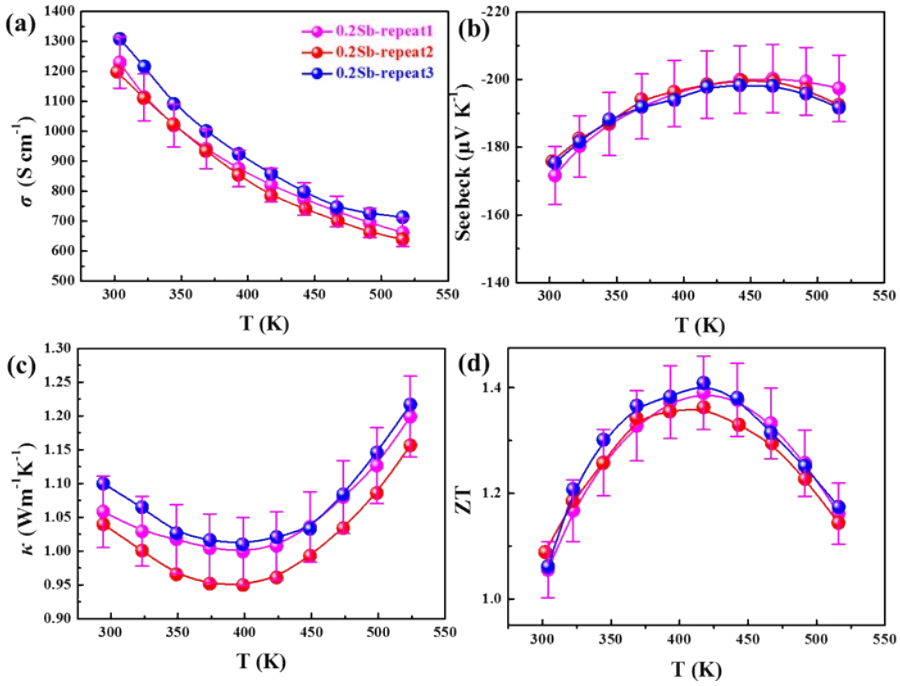

Figure S11 The temperature dependence of (a) electrical conductivity, (b) Seebeck coefficient (c) thermal conductivity and (d) ZT values for repeat 0.2Sb sample.

In order to insure the accuracy of our data, I have prepared 0.2Sb sample three times, and their TE properties are shown in the **Figure S11**. The error bars in Figure S10 are machine errors, which are widely accepted in TE society. As can be seen, TE properties of the repeat samples are closed to each other and within the error bars. Therefore, we can conclude our data is reliable and accurate.

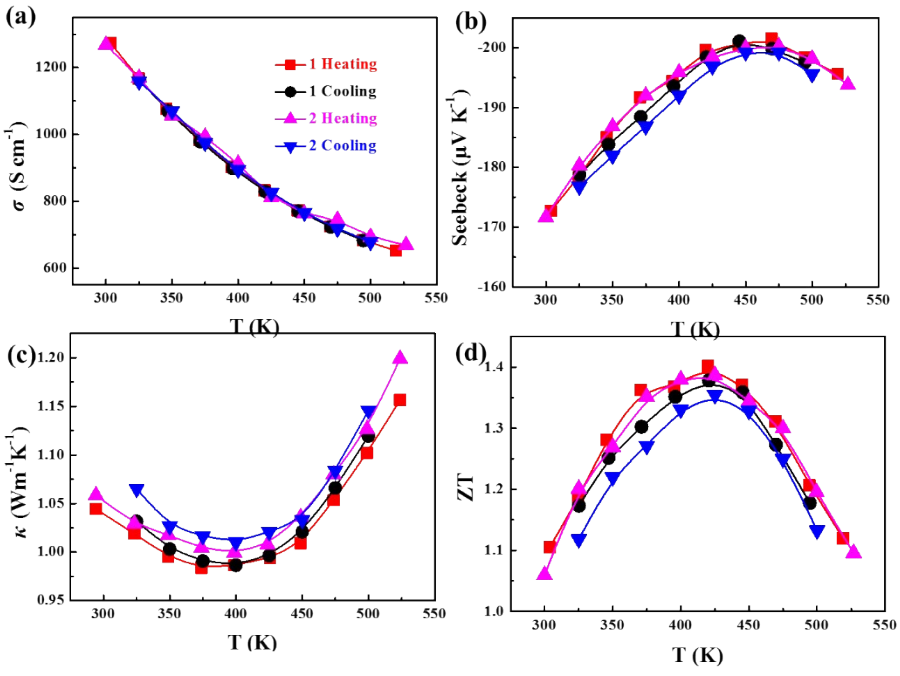

Figure S12 The cycle measurement for 0.2Sb sample.

The cycling measurement has also been carried out, as shown in **Figure S12**. After 2 heating-cooling cycle measurement (about 20 hours), the maximum still over 1.3, which suggest a good cyclability.

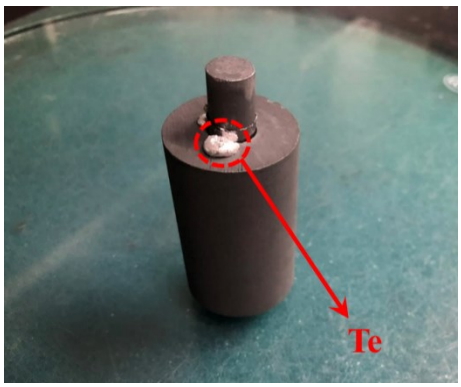

Figure S13 The image of squeezed out Te**.**

The calculation of κ_l

The Callaway model

$$k_L = \frac{k_B}{2\pi^2 v_{avg}}\left(\frac{k_B T}{\hbar}\right)^3 \int_0^{\theta_D/T} \frac{x^4 e^x}{\tau_C^{-1}(e^x-1)^2}dx \qquad \text{(S8)}$$

where $x = \hbar\omega/k_B T$ is the reduced phonon frequency, w is the phonon frequency, κ_B is the Boltzmann constant, $\hbar$ is the reduced Planck constant, w_D is the Debye temperature, and τ_C is the overall phonon scattering relaxation time. Six phonon scattering mechanisms are considered here, including phonon-phonon Umklapp scattering (U), Grain boundary scattering (GB), point defect scattering (PD), dislocation strain scattering (DS), dislocation core scattering (DC) and nano precipitate scattering (P). The overall phonon scattering relaxation time is expressed as

$$\tau_C^{-1} = \tau_{GB}^{-1} + \tau_U^{-1} + \tau_{PD}^{-1} + \tau_{DS}^{-1} + \tau_{DC}^{-1} + \tau_P^{-1} \qquad \text{(S9)}$$

For common grain boundary, there is perfect acoustic mismatch at the interface between the material and vacuum, the relaxation times of phonons will be independent with the phonon frequency. The frequency-independent τ_{GB} is given by

$$\tau_{GB}^{-1} = \frac{v}{d} \quad \text{(S10)}$$

Where v is the average sound velocity and d is the experimentally determined grain size. Umklapp scattering occurs when phonons in a crystal are scattered by other phonons. Its relaxation time is of the form

$$\tau_{U}^{-1} = A_N \frac{2}{(6\pi^2)^{1/3}} \frac{k_B V^{1/3} \gamma^2 \omega^2 T}{M v^3} \quad \text{(S11)}$$

Where *V,* γ, and *M* are the atomic volume, Gruneisen parameter, and the atomic mass. The parameter A_N takes normal phonon-phonon scattering (total crystal momentum conserving process) into account. Point-defect scattering arises from an atomic size disorder in alloys. The disorder is described in terms of the scattering parameter (Γ) within the τ_{PD} formula as

$$\tau_{PD}^{-1} = \frac{V\omega^4}{4\pi v^3}\Gamma \quad \text{(S12)}$$

Γ is related to the difference in mass (ΔM) and lattice constant (Δa) between two constituents of an alloy.

For a material with dislocations, the scattering caused by the dislocations strain and cores(DS) should be considered. Relaxation time of dislocation scattering can be considered [3]

$$\tau_{DS}^{-1} = N_D \frac{\bar{V}^{\frac{4}{3}}}{v^2}\omega^3 + 0.6 B_D^2 N_D (\gamma + \Delta\gamma)^2 \omega \left\{ \frac{1}{2} + \frac{1}{24}\left(\frac{1-2r}{1-r}\right)^2 \left[1 + \sqrt{2}\left(\frac{v_L}{v_T}\right)\right]^2 \right\} \quad \text{(S13)}$$

N_D, B_D, γ, $\Delta\gamma$, r, v_L, v_T are dislocation density, effective Burger's vector, Grüneisen parameter, change in Grüneisen parameter due to the dislocation strain , Poisson's ratio, longitudinal phonon velocity and transverse phonon velocity, respectively. $\Delta\gamma$ can be expressed as

$$\Delta\gamma = \frac{V_{BT} C_0 K}{K_B T_a}(\gamma\alpha^2 - \alpha\beta) \quad \text{(S14)}$$

$$\alpha = \frac{V_{BS} - V_{BT}}{V_{BT}} \quad \text{(S15)}$$

$$\beta = \frac{M_{BT} - M_{BS}}{2M_{BT}} \quad \text{(S16)}$$

Where C_0 is the concentration of Bi_2Se_3 in $Bi_2Te_{3-x}Se_x$, K is the bulk modulus of Bi_2Te_3, Ta is the sample smelting temperature, V_{BS} and V_{BT} are the atomic volume of Bi_2Se_3 and Bi_2Te_3, and M_{BS} and M_{BT} are the atomic mass of Bi_2Se_3 and Bi_2Te_3.

For nanoscale precipitate, the relaxation time of nano precipitate can be expressed as:

$$\tau_P^{-1} = v(\sigma_s^{-1} + \sigma_l^{-1})^{-1} V_P \quad \text{(S17)}$$

$$\sigma_s = 2\pi R^2 \quad \text{(S18)}$$

$$\sigma_l = \frac{4}{9}\pi R^2 \left(\frac{\Delta D}{D_{matrix}}\right)^2 \left(\frac{\omega R}{v}\right)^4 \quad \text{(S19)}$$

$$\Delta D = D_{matrix} - D_{precipitate} \quad \text{(S20)}$$

Where v, V_p, R, D_{matrix} and $D_{precipitate}$ are average sound speed, number density of nano precipitates, average radius of the precipitates, mass density of matrix and precipitates respectively.

To use this corrected Callaway's model to calculate the lattice thermal conductivity, all the parameters should be fixed based on experimental results. But the parameter A_N used to calculate the τ_U can't be fixed based on experimental data, which takes normal phonon-phonon scattering (total crystal momentum conserving process) into account. Thus we use the in-plane lattice thermal conductivity of full dense, large grained ZM $Bi_2Te_{2.7}Se_{0.3}$ sample to calculate the parameter A_N. Compared with the ZM ingots, the grains of our samples are much refined, the effect of grain boundary on depressing lattice thermal conductivity are calculated and shown in the blue dash line of Figure 4(b). Similarly, the depressed lattice thermal conductivity from the dislocation and precipitate have also been calculated and plotted in Figure 4(a). We can concluded that the dislocation and nanoscale precipitate result in as much as ~50% and 30% total reduction of lattice thermal conductivity. Meanwhile, the frequency dependence of phonon scattering process has also been calculated and shown in Figure 4(b). The conclusion is that the grain boundary (plane defect) and point defect will scatter

phonons in the low and high range respectively. While the dislocation (line defect) and nanoscale precipitate scatter phonons in the low and middle range. These plane, line and point defects could scatter whole range phonons and decrease lattice thermal conductivity as large as possible. And all the parameters are listed in the Table S1.

The calculation of theory efficiency:

The theory efficiency of TE module could be given as following equations:

$$\eta_{max} = \frac{T_H - T_C}{T_H} \frac{(1+\bar{Z}T)^{1/2} - 1}{(1+\bar{Z}T)^{1/2} + T_C/T_H} \quad \text{(S21)}$$

$$\bar{Z} = \left(\frac{\bar{S}_P + \bar{S}_N}{\sqrt{\bar{\kappa}_P/\bar{\sigma}_P}\sqrt{\bar{\kappa}_N/\bar{\sigma}_N}} \right)^2 \quad \text{(S22)}$$

$$\bar{S} = \frac{1}{T_H - T_C} \int_{T_C}^{T_H} S(T)dT \quad \text{(S23)}$$

$$\bar{\sigma} = \frac{1}{T_H - T_C} \int_{T_C}^{T_H} \sigma(T)dT \quad \text{(S24)}$$

$$\bar{\kappa} = \frac{1}{T_H - T_C} \int_{T_C}^{T_H} \kappa(T)dT \quad \text{(S25)}$$

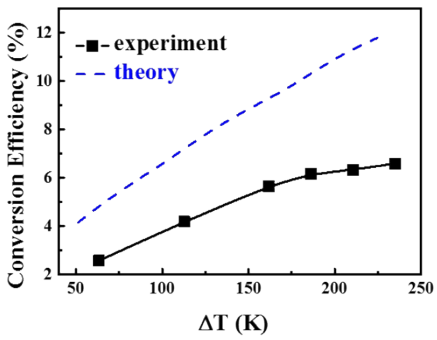

Figure S14 The comparison of experiment and theory conversion efficiency.

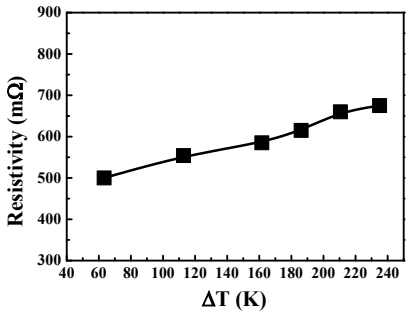

Figure S15 The resistivity for TE module

Table. S1 Physical properties used to calculate κ_l based on various phonon scattering processes

Parameters	Values
Debye temperature θ_D (K)	164[4]
Parameter A_N	1.5
Longitudinal sound velocity υ_L(ms^{-1})	2800[4]
Transverse sound velocity υ_T (ms^{-1})	1600[4]
Sound velocity υ(ms-1)	1778
Average atomic mass of Bi_2Te_3 M_{BT} (kg)	2.66×10^{-25}
Average atomic mass of Bi_2Se_3 M_{BS} (kg)	2.18×10^{-25}
Average atomic volume of Bi_2Te_3 V_{BT} (m^3)	3.48×10^{-29}
Average atomic volume of Bi_2Se_3 V_{BS} (m^3)	3.19×10^{-29}
Sample density ρ (g cm^{-3})	7.28
Grain size d (um)	10
number density of nano precipitates V_p (m^{-3})	2.55×10^{20}
Point defect scattering parameter Γ	0.23
Dislocation density ND of $Bi_2Te_{2.7}Se_{0.3}$ (cm^{-2})	1.5×10^{11}
Average radius of nanoscale precipitates R (nm)	20
Mass density of matrix D_{matrix} (g/cm^3)	7.8
Mass density of nanoscale precipitates $D_{precipitate}$ (g/cm^3)	6.7
Number density of nanoscale precipitates V_P (m-3)	2×10^{20}
Magnitude of Burger's vector BD	12
Poisson's ratio r	0.14[5]
Grüneisen parameter γ	1.5[6]
Bulk modulus K (GPa)	37.4[4]

Table S2: Calculated parameter *A* and by *B* using the minor and major carrier concentration at 300 K.

Samples	0Sb	0.1Sb	0.2Sb
A(10^{30}cm^{-6})	2.58	2.68	3.12
B	121.1	116.5	119.2

References

1. F. K. Lotgering, *J. Inorg. Nucl. Chem.*, 1959, **9**, 113-123.
2. X. S. Rigui Deng, Zheng Zheng, Wei Liu, Yonggao Yan, Qingjie Zhang, Vinayak P. Dravid, Ctirad Uher, Mercouri G. Kanatzidis, Xinfeng Tang, *Sci. Adv.*, 2018, **4**, 1-8.
3. S. I. Kim, K. H. Lee, H. A. Mun, H. S. Kim, S. W. Hwang, J. W. Roh, D. J. Yang, W. H. Shin, X. S. Li, Y. H. Lee, G. J. Snyder and S. W. Kim, *Science*, 2015, **348**, 109-114.
4. J. Jenkins, J. Rayne and R. Ure Jr, *Phy. Rev. B*, 1972, **5**, 3171.
5. T. Clin, S. Turenne, D. Vasilevskiy and R. Masut, *J. Electron. Mater.*, 2009, **38**, 994-1001.
6. X. Chen, H. Zhou, A. Kiswandhi, I. Miotkowski, Y. Chen, P. Sharma, A. Lima Sharma, M. Hekmaty, D. Smirnov and Z. Jiang, *Appl. Phys. Lett.*, 2011, **99**, 261912.